THE JOURNAL OF PHYSICAL CHEMISTRY C

Article

pubs.acs.org/JPCC

Dependence of Nanocrystal Dimensionality on the Polymer Nanomorphology, Anisotropic Optical Absorption, and Carrier Transport in P3HT:TiO_2 Bulk Heterojunctions

Chih-Cheng Lin,[†] Po-Hsun Ho,[†] Chi-Liang Huang,[‡] Chao-Hung Du,[‡] Chen-Chieh Yu,[†] Hsuen-Li Chen,[†] Yun-Chieh Yeh,[†] Shao-Sian Li,[†] Cheng-Kuang Lee,[§] Chun-Wei Pao,[§] Ching-Pin Chang,[∥] Ming-Wen Chu,[∥] and Chun-Wei Chen*[,†]

[†]Department of Materials Science and Engineering, National Taiwan University, Taipei, 10617, Taiwan

[‡]Department of Physics, Tamkang University, Tamsui, 25137, Taiwan

[§]Research Center for Applied Sciences, Academia Sinica, Nankang, 11529, Taiwan

[∥]Center for Condensed Matter Sciences, National Taiwan University, Taipei, 10617, Taiwan

Supporting Information

ABSTRACT: It is known that the nanoscale morphological organization of donors or acceptors in bulk heterojunction (BHJ) solar cells is critical to device performance and strongly affects carrier generation, transporting, and collection. This work demonstrates the dependence of nanocrystal dimensionality and organization on the polymer nanomorphology in P3HT:TiO_2 hybrid bulk heterojunctions, which were revealed using grazing-incidence X-ray diffraction (GIXRD) using a synchrotron X-ray beam and electron tomography. We further performed a multiscale molecular dynamic simulation to understand the morphological orientation of a polymer blended with TiO_2 nanoparticles (NPs) or nanorods (NRs). The correlation between polymer nanoscale morphology and the dimensionality and anisotropy of nanocrystals in P3HT:TiO_2 hybrids clearly explains the observation of different optical absorption and carrier transport behaviors in directions perpendicular or parallel to the film substrate. Our results provide crucial information toward understanding the interplay between nanocrystal dimensionality and polymer morphology in developing organic/inorganic hybrid electronic devices such as thin film transistors (TFTs) or photovoltaics (PVs).

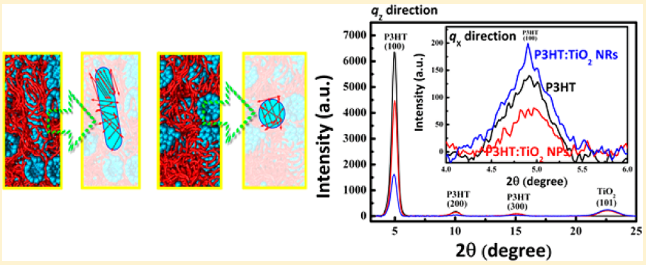

1. INTRODUCTION

Polymer solar cells[1−3] have attracted considerable interest for fabricating low-cost and mechanically flexible photovoltaic devices over the past decade, benefiting from the possibility of solution processing and patterning on flexible substrates. The most promising device structure of polymer solar cells is based on bulk heterojunctions (BHJs), which consist of interpenetrating networks using electron-donor and electron-acceptor components, creating the donor/acceptor interfaces for efficient exciton dissociation and charge transport. Extensive research has focused on developing polymer photovoltaic devices using fullerene or fullerene derivatives as acceptors, and recent advances in achieving high photovoltaic efficiencies near 7−8% have been realized.[4,5] An alternative type of polymer solar cell, based on a polymer/inorganic nanocrystal hybrid device structure, is also appealing because of relatively high electron mobility as well as good physical and chemical stability of inorganic nanocrystals. Various inorganic nanocrystals, such as CdSe,[6] PbS,[7] ZnO,[8] and TiO_2,[9] have been used in polymer/inorganic hybrid BHJ solar cells. Because nanoscale morphologies of inorganic nanocrystals can vary, from well-dispersed nanoparticles (NPs) or nanorods (NRs),[6] nanotetrapods,[10] to well-connected nanoporous[11] or aligned ordered nanostructures grown directly on substrates,[12] the morphologies of the active layers consisting of polymer/inorganic nanocrystal BHJs vary considerably from those of the conventional polymer photovoltaic devices using fullerene or fullerene derivatives as acceptors.[13] Because of the strong incompatibility between inorganic nanocrystals and polymers, the precarious control of the BHJ morphology of the two intermixed components becomes particularly challenging. We demonstrated a promising power conversion efficiency for photovoltaic devices consisting of poly(3-hexylthiophene) (P3HT):TiO_2 NR BHJs by performing an interface modification,[9] and the significant improvement of compatibility between P3HT and TiO_2 NRs by replacing interfacial ligand molecules results in efficient charge transfer and suppression of charge recombination at polymer/nanocrystal interfaces. In addition, it is known that the

Received: July 12, 2012
Revised: October 26, 2012
Published: November 5, 2012

   dx.doi.org/10.1021/jp306921e | J. Phys. Chem. C 2012, 116, 25081−25088

nanoscale morphological organization of donors or acceptors in BHJ solar cells is also critical to the device performance and strongly affects carrier generation, transporting, and collection. Recently, morphological organizations of TiO_2 NPs and NRs blended with poly(3-hexylthiophene) (P3HT) were revealed by our group employing electron tomography based on scanning transmission electron microscopy using high-angle annular dark-field imaging (STEM-HAADF),[14] which provides the critical morphological parameters for improving device performance.[15−17] Although the unambiguous experimental evidence confirming the three-dimensional nanocrystal morphological organization in P3HT:TiO_2 hybrid has been realized, the detailed morphological information on conjugated polymer within the polymer/inorganic BHJ systems is still limited thus far. In this work, we investigated the nanoscale morphological orientation of polymer in P3HT:TiO_2 BHJs by employing state-of-art grazing-incidence X-ray-diffraction (GIXRD) measurements using a synchrotron X-ray beam. Because of the influences of nanocrystal dimensionality and organization, the polymer chains in P3HT:TiO_2 NP and NR BHJs showed different morphological orientations in directions parallel and perpendicular to the substrate surface. A multiscale molecular dynamic simulation employing coarse-grained molecular dynamics (CGMD) simulation was also used to model the nanoscale morphology of P3HT:TiO_2 nanocrystal blends to explain the observed experimental results. The effect of nanocrystal dimensionality on the polymer nanomorphology in P3HT:TiO_2 hybrids was further manifested from their anisotropic optical absorption and carrier transport behaviors, which provide crucial information in developing organic/inorganic hybrid electronic devices such as thin film transistors (TFTs) or photovoltaics (PVs).

2. EXPERIMENTS

We prepared both P3HT:TiO_2 NP and P3HT:TiO_2 NR hybrid thin films with a weight ratio of 50:50 (wt %), according to a previous report.[9] The TiO_2 nanocrystals have characteristic sizes of ∼5 nm for the NPs and ∼4 nm (diameter) × ∼20 nm (length) for the NRs, as shown in Figures S1a and S1b of the Supporting Information. The ligand-exchange treatment using pyridine on both TiO_2 NPs and NRs was further used to remove the original oleic acid (OA) surfactant to improve the compatibility between P3HT and TiO_2 nanocrystals.[9] The hybrid films were spin-coated on the substrate by using the 1:1 weight ratio of P3HT:TiO_2 NP and NR blends which corresponds to the optimized ratio in the photovoltaic device,[14] dissolved in 1,2,4-trichlorobenzene. The transmission electron microscopy (TEM) images of P3HT:TiO_2 NPs and P3HT:TiO_2 NRs films are shown in Figures S1d and S1e of the Supporting Information, respectively. For optical anisotropic measurements, ellipsometric parameters (tan Ψ and cos Δ) were acquired using a SOPRA ellipsometer. Transmittance and reflectance spectra were recorded using a Hitachi U-4100 optical spectrometer at various incident angles. The measured data were fit to a dispersion function, also called an oscillator model to describe both real and imaginary parts of the refractive index over a wide spectral range. GIXRD measurements were carried out on the wiggler beamline BL17A1 of National Synchrotron Radiation Research Center (NSRRC, Taiwan), with a wavelength of 1.3302 Å. All the samples were spin-coated on the heavily boron-doped silicon substrate. In order to increase the effective X-ray penetrating depth and minimize the background from the substrate scattering, the angle between the incident beam and the film surface was fixed at 0.2°. The data were recorded by an online image plate Mar345 and analyzed using FIT-2D software. STEM tomography experiments were conducted on a field-emission microscope operated at 200 keV (FEI F20 G^2) with an electron-probe size of ∼2 Å.[14] The three-dimensional (3D) reconstructions of these two-dimensional (2D) STEM-HAADF data sets were performed using the weighted back-projection algorithm integrated in the FEI Inspect3D software package, and further 3D visualization artworks were conducted using AMIRA 4.0 (Mercury Computer Systems).

In the coarse-grained molecular dynamics (CGMD) simulation of P3HT:TiO_2 NP and NR blends, we fitted a CG force field model based on molecular trajectories from all-atom molecular dynamics simulations. The details of fitting CG force field in P3HT:TiO_2 NPs and NRs system can be found elsewhere.[18] In brief, for the CG model of P3HT, each P3HT repeated unit was coarse-grained into a CG bead, and the CG force fields between CG beads were fitted to reproduce the distribution of CG degrees of freedom and radial distribution functions from all-atom molecular dynamics simulations. For the CG model of TiO_2 nanocrystals, TiO_2 NP and NR with given sizes were mapped into clusters of CG particles, and the CG force fields between CG particles were fitted to reproduce the potential energy surface between two TiO_2 NPs or NRs from all-atom molecular dynamics simulations. We carried out CGMD simulations under the NPT ensemble condition with a system size of 60 × 60 × 60 nm^3 at 1 atm and T = 423 K. Periodic boundary conditions were applied along all directions of simulation cells. The molecular dynamics simulation package DL_POLY4[19] was employed for all the CGMD simulations.

To measure the carrier mobility along the direction perpendicular to the substrate, the hole-only and electron-only devices for space-charge-limited-current (SCLC) measurements were fabricated by spin-coating the active layer with the thickness of ∼150 nm between top and bottom electrodes. For hole-only device, thermally evaporated Au and ITO substrate coated with PEDOT:PSS were used because their work function levels match the HOMO level of P3HT. For electron-only device, Al was used for both top and bottom electrode to match the LUMO level of TiO_2. The vertical carrier mobility are examined from the typical current density−voltage (J−V) characteristics according to the Mott−Gurney law:[20]

$$J = \frac{9}{8}\varepsilon\varepsilon_0\mu\frac{V_{\mathrm{eff}}{}^2}{L^3} \quad (1)$$

where J is the hole or electron current density, ε_0 is the vacuum permittivity, and ε is the dielectric constant of P3HT (2.5) or TiO_2 (50).[21] μ is the hole or electron mobility, and L is the thickness of active layer. The effective voltage drop (V_{eff}) within the active layer is expressed as

$$V_{\mathrm{eff}} = V_{\mathrm{applied}} - V_{\mathrm{bi}} - V_{\mathrm{Rs}} \quad (2)$$

where V_{bi} is the built-in voltage drop caused by the work function difference between electrodes and V_{Rs} is the voltage drop induced by the series resistance of device.

To measure the hole field-effect mobility along the direction horizontal to the substrate, thin film transistors (TFTs) were fabricated on highly boron-doped (100) Si substrate (0.01−0.005 Ω cm) with 300 nm thermally grown silicon dioxide (SiO_2). The octadecyltrichlorosilane (OTS)-treated SiO_2

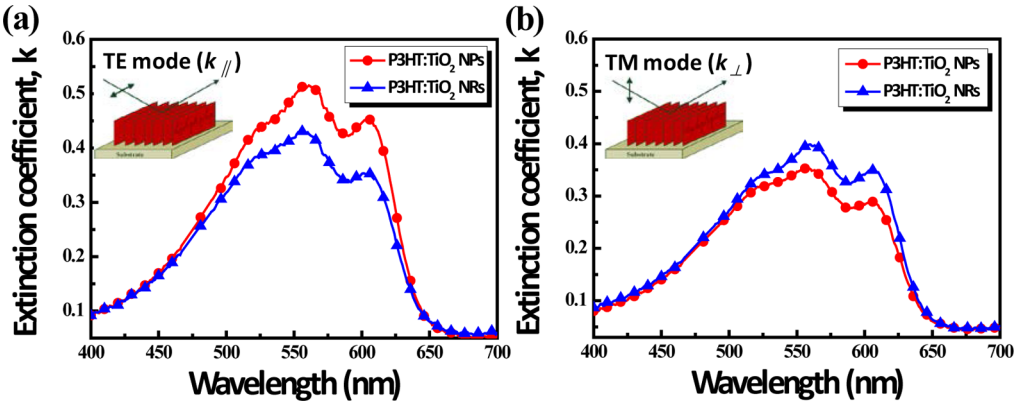

Figure 1. Optical extinction coefficients of the P3HT:TiO_2 NPs and P3HT:TiO_2 NRs hybrids (a) in the TE mode and (b) in the TM mode. The insets show schematic representations for the direction of the electric field of incident light with respect to the substrate.

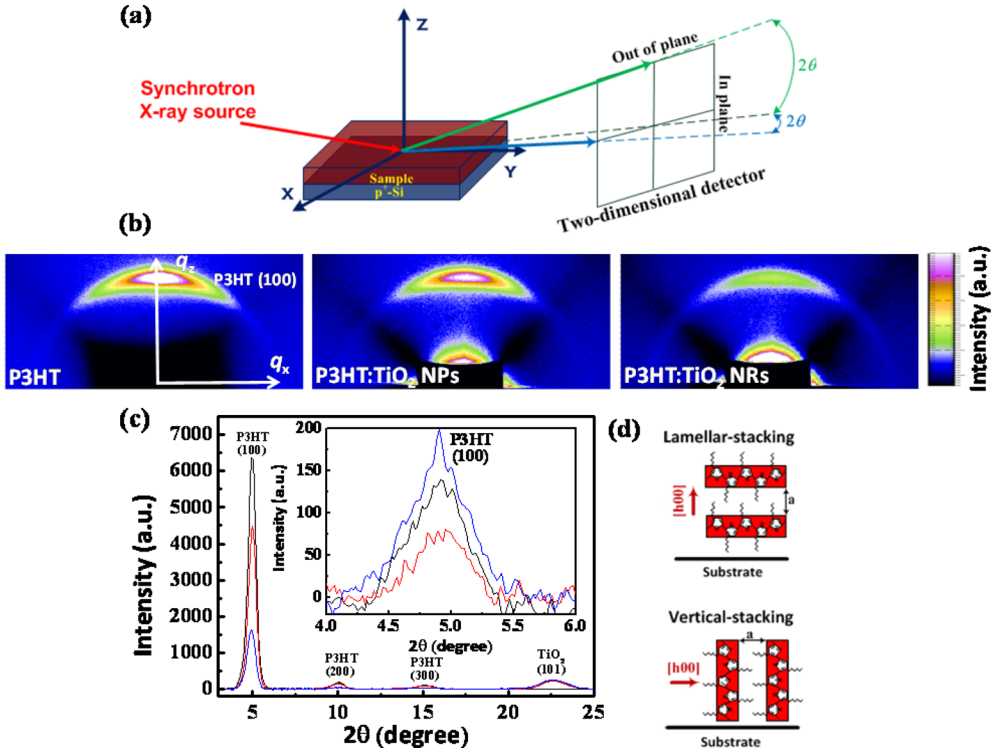

Figure 2. (a) Scheme of GIXRD setup (λ = 1.3302 Å) for out-of-plane and in-plane measurements. (b) 2D GIXRD images of pristine P3HT film, P3HT:TiO_2 NPs and P3HT:TiO_2 NRs hybrids. 1D plot of XRD patterns are shown in the (c) out-of-plane (q_z) and in-plane (q_x) (as shown in the inset of (c)) directions. Black, red, and blue curves represent pristine P3HT film, P3HT:TiO_2 NPs, and P3HT:TiO_2 NRs hybrids, respectively. (d) Illustrations of the lamellar stacking and vertical stacking of P3HT crystallites with respect to the substrate surface.

surface was used to modify the substrate as reported in the previous study.[22] After the BHJs films were spin-coated at 1000 rpm on the OTS-treated substrate, the source and drain electrodes were evaporated a 60 nm thick Au layer onto the film through a shadow mask, defining 100 μm length and 1.2 mm width of channels, to fabricate top-contact TFTs. Finally, these devices were annealed at 120 °C for 6 h under vacuum to remove residual solvent. The field-effect hole mobility operated in a saturated regime by using the standard saturation equation:

$$I_{DS} = \frac{W}{2L}\mu_{sat}C_{ox}(V_G - V_T)^2 \quad (3)$$

where I_{DS}, W, L, and μ_{sat} are the saturated drain current, the channel width, the channel length, and the saturated field-effect mobility, respectively.

3. RESULTS AND DISCUSSION

We first used ellipsometry measurements to characterize the anisotropic absorption intensities of the P3HT:TiO_2 NP and P3HT:TiO_2 NR hybrids, as shown in Figure 1. Using the reflectance and transmittance spectra of polarized light at various incident angles, the TE polarized curve was fitted to acquire the in-plane extinction coefficient ($k_{\parallel}$); the TM polarized curve was then fitted to obtain the out-of-plane extinction coefficient ($k_{\perp}$). As shown in Figure 1a, the extinction coefficient $k_{\parallel}$ in the TE polarized incidences for the P3HT:TiO_2 NP hybrid is higher than that of the P3HT:TiO_2 NR hybrid counterpart. By contrast, the extinction coefficient $k_{\perp}$ in the TM polarized incidences for the P3HT:TiO_2 NR hybrid is higher than that of the P3HT:TiO_2

dx.doi.org/10.1021/jp306921e | J. Phys. Chem. C 2012, 116, 25081−25088

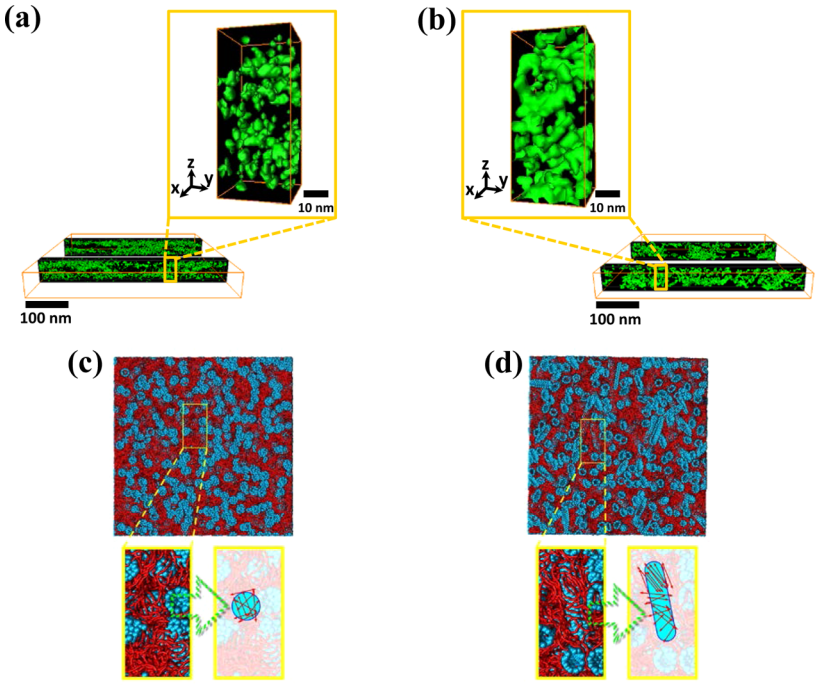

Figure 3. STEM-HAADF electron tomography images of the (a) P3HT:TiO_2 NPs and (b) P3HT:TiO_2 NRs hybrids. These images with dark (green) contrasts represent light (heavy) matter, that is, P3HT for the dark contrast and TiO_2 for the green contrast. Three-dimensional morphologies of (c) P3HT:TiO_2 NPs and (d) P3HT:TiO_2 NRs blends using coarse-grained molecular dynamics (CGMD) simulations. TiO_2 CG nanocrystals are colored in blue, and P3HT CG chains are colored in red.

NP hybrid, as shown in Figure 1b. The electric field of incident light aligned parallel to the direction of P3HT thiophene chains (i.e., the orientation of transition dipole moments) usually results in stronger $\pi-\pi^*$ absorption.[23,24] This optical anisotropic absorption result suggests that the orientations of polymer chains in P3HT:TiO_2 NP and P3HT:TiO_2 NR hybrids might be quite different.

To investigate how the orientations of polymer chains were influenced by the nanocrystal size or dimensionality, we employed the GIXRD measurements using a synchrotron X-ray beam to further examine the nanoscale morphologies of polymer chains in P3HT:TiO_2 nanocrystal hybrids. For comparison, the measurement for the pristine P3HT film was also performed. Figure 2a shows the typical setup of the GIXRD measurement. Figure 2b shows the two-dimensional GIXRD images for these films consisting of pristine P3HT, P3HT:TiO_2 NP, and P3HT:TiO_2 NR hybrids, respectively. These images consist of two crystallographic components, q_x and q_z, where q_x corresponds to the in-plane direction of the substrate and q_z is the out-of-plane direction normal to the substrate surface. The GIXRD profiles, which were integrated along out-of-plane (q_z) and in-plane (q_x) directions, are shown in Figure 2c and in its inset, respectively. First, the appearance of a TiO_2 (101) diffraction peak (diffraction angle at 2θ = 22.6°) in the out-of-plane (q_z) direction is consistent with the typical XRD signature of anatase TiO_2 crystals, as shown in Figure S1c of the Supporting Information. In addition, both the (101) diffraction intensities of TiO_2 nanocrystals in P3HT:TiO_2 NP and P3HT:TiO_2 NR hybrids are almost identical, as a result of same amounts of TiO_2 nanocrystal in hybrid films. The lamellar-stacking (edge-on) structure of P3HT (as shown in the top panel of Figure 2d), corresponding to P3HT thiophene chains with alkyl stacking normal to the substrate,[25] usually provides the (h00) diffraction peak in the out-of-plane (q_z) direction; by contrast, the vertical structure of P3HT (as shown in the bottom panel of Figure 2d), corresponding to P3HT thiophene chains stacking normal to the substrate,[25] usually shows a (h00) diffraction peak in the in-plane (q_x) direction. We found that the (100) peak intensity (diffraction angle at 2θ = 4.99°) in the out-of-plane (q_z) direction for the P3HT:TiO_2 NR hybrid is much lower than that for the P3HT:TiO_2 NP counterpart. However, the trend of the (100) diffraction intensities in the in-plane (q_x) direction (inset of Figure 2c) is noticeably different from that of the (100) diffraction intensities in the out-of-plane (q_z) direction, where the P3HT:TiO_2 NR hybrid sample shows a stronger peak intensity of (100) diffraction in the in-plane (q_x) direction. The result indicates that the morphology and chain orientation of polymer strongly depend on the nanocrystal dimensionality in P3HT:TiO_2 bulk heterojunctions, consistent with the above observation of a higher extinction coefficient $k_\perp$ in P3HT:TiO_2 NR hybrid with respect to the P3HT:TiO_2 NR counterpart. As we further compared the diffraction peak intensities of the P3HT:TiO_2 NR hybrid sample with those of the pristine P3HT film, we found that the peak intensity of (100) diffraction in the in-plane (q_x) direction for the P3HT:TiO_2 NR hybrid sample is also higher although its (100) diffraction peak in the out-of-plane (q_z) direction is much lower than that of the pristine P3HT. The decreased (100) peak intensity in the out-of-plane (q_z) direction for the P3HT:TiO_2 NR hybrid indicates that the lamellar stacking of P3HT crystallites within P3HT:TiO_2 hybrid was reduced after adding TiO_2 nanocrystals. A similar observation in P3HT:PCBM thin films with increasing amounts of PCBM has also been reported.[26] However, the enhanced (100) peak intensity in the in-plane (q_x) direction of P3HT:TiO_2 NR hybrid sample with respect to the pristine P3HT suggests the possible formation of increased vertical stacking of P3HT crystallites after adding TiO_2 NRs into

dx.doi.org/10.1021/jp306921e | J. Phys. Chem. C 2012, 116, 25081−25088

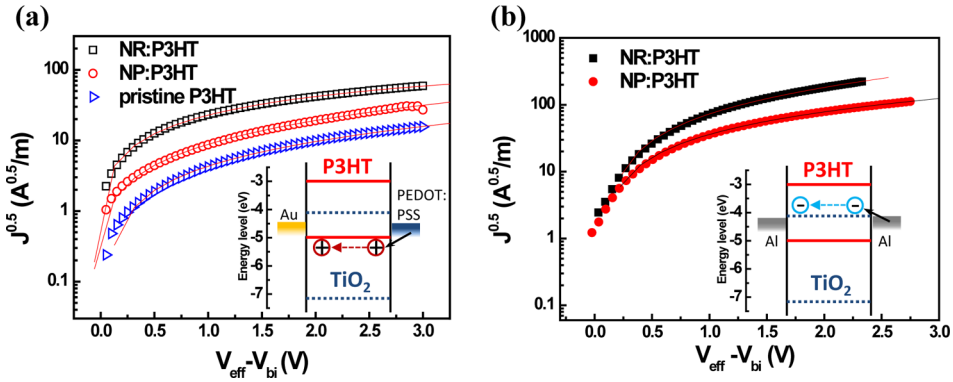

Figure 4. Space charge limited current (SCLC) for (a) hole-only and (b) electron-only devices. The insets show the energy levels of both types of device.

P3HT. No enhancement with the same diffraction peak of the P3HT:TiO_2 NP hybrid sample was observed. A similar trend for the P3HT:TiO_2 NR and NP hybrids with various TiO_2 loading ratios was also observed (see the Supporting Information). Previous studies have also reported the enhanced vertical chain alignment of P3HT infiltrated into ordered nanostructures using straight nanopores of anodic alumina[27] or nanoimprint lithography.[28] Figures 3a and 3b show the slices through the reconstructed volumes of the three-dimensional morphological organizations of TiO_2 NPs and TiO_2 NRs along the vertical direction in P3HT:TiO_2 BHJs, as revealed using electron tomography. Although TiO_2 NRs do not form ordered nanostructures in P3HT:TiO_2 BHJs, the aspect ratio of the TiO_2 NRs with preferred orientations angled toward the plane of the film might allow for the self-alignment of polymer chains along the TiO_2 NR surface, as observed in the systems consisting of straight nanopores[27] or nanowire,[29] resulting in an overall enhancement in the vertical stacking of P3HT and a decrease in the lamellar stacking. By contrast, the isotropic TiO_2 NPs without any preferred orientation does not cause such an enhancement in P3HT:TiO_2 NP BHJs. To further understand the morphological orientation of a polymer blended with TiO_2 NPs or NRs, we performed a multiscale CGMD simulation based on the technique we developed earlier for polymer:fullerene blends.[18] The details of the simulation method are described in the Experiments section. Figures 3c and 3d display the morphologies of P3HT:TiO_2 NP and P3HT:TiO_2 NR hybrids with a blending ratio of 1:1 derived from our CGMD simulations. Close examination of Figures 3c and 3d further reveals the organization of P3HT chains near the TiO_2 NP and TiO_2 NR surface, as shown in the blow-up regions enclosed in the yellow boxes. For the P3HT:TiO_2 NP blend, it is clear that P3HT bond vectors (red arrows in the lower-right panel of Figure 3c) do not have a preferential direction. By contrast, for the P3HT:TiO_2 NR blend, substantial P3HT chains prefer aligning along the axial direction of TiO_2 NRs (as shown in the lower-right panel of Figure 3d). From the CGMD simulation result, we can verify that the elongated and anisotropic TiO_2 NRs with preferred orientations angled toward the plane of the film tend to promote the formation of self-aligned P3HT crystallites along the rod axis, which is consistent with the observed higher extinction coefficient $k_\perp$ and enhancement of the in-plane (q_x) (100) diffraction peak intensity in P3HT:TiO_2 NR hybrid. This result indicates that the orientation of P3HT polymer in P3HT:TiO_2 nanocrystal hybrids strongly depends on the dimensionality and anisotropy of TiO_2 NPs or NRs.

It is well-known that carrier mobility of conjugated polymer is largely influenced by the polymer chain orientation.[30,31] Therefore, we investigated the hole transport behaviors in P3HT:TiO_2 nanocrystal hybrids along the directions perpendicular or parallel to the substrate. We first fabricated the hole-only devices made from pristine P3HT, P3HT:TiO_2 NP, and P3HT:TiO_2 NR hybrids using the space-charge-limited current (SCLC) measurement to estimate the hole mobility along the direction perpendicular to the substrate. In these devices, ohmic contact for hole injection was achieved using a gold top electrode and a PEDOT:PSS/ITO bottom electrode. Figure 4a shows the square root of the hole current density ($J_h^{1/2}$) versus the effective voltage (V_{eff}) characteristics of pristine P3HT, P3HT:TiO_2 NP, and P3HT:TiO_2 NR-based devices. The details of the model for SCLC mobility measurement are described in the Experiments section. Both the P3HT:TiO_2 NP and NR-based devices exhibit higher hole current densities, as compared to the pristine P3HT device. The estimated hole mobilities of pristine P3HT, P3HT:TiO_2 NP, and P3HT:TiO_2 NR hybrids are 3.01×10^{-5}, 1.18×10^{-4}, and 3.98×10^{-4} cm^2 V^{-1} s^{-1}, respectively. Because TiO_2 nanocrystals usually demonstrate highly effective hole blocking,[32] establishing separated P3HT and TiO_2 nanocrystal transport pathways allows the holes to move along the confined P3HT domains surrounded by the TiO_2 nanocrystals to reduce recombination and facilitate transport.[14] In addition, the higher SCLC hole mobility of P3HT:TiO_2 NR hybrid, as compared to that of the P3HT:TiO_2 NP counterpart, is consistent with the increased vertical stacking of P3HT crystallites between two electrodes caused by partially aligned polymer chains along the anisotropic TiO_2 NRs. This enables the hole transport in P3HT:TiO_2 NR hybrid along the direction normal to the substrate to be more effective than that in P3HT:TiO_2 NP hybrid counterpart. We also fabricated the electron-only devices based on P3HT:TiO_2 NR and P3HT:TiO_2 NP hybrids. Figure 4b shows the SCLC current−voltage curves of the electron-only devices consisting of P3HT:TiO_2 NR and NP hybrids with the device configuration of Al/P3HT:TiO_2/Al as shown in the inset. An energy barrier was created between Al electrode and HOMO level of P3HT, which prevents the injection of hole carriers, to form an electron-only device structure. The electron mobility in the P3HT:TiO_2 NR hybrid device is 2.35×10^{-4} cm^2 V^{-1} s^{-1} while it is 4.25×10^{-5} cm^2 V^{-1} s^{-1} in the P3HT:TiO_2 NP hybrid device. The resulting hole mobility to electron mobility

dx.doi.org/10.1021/jp306921e | J. Phys. Chem. C 2012, 116, 25081−25088

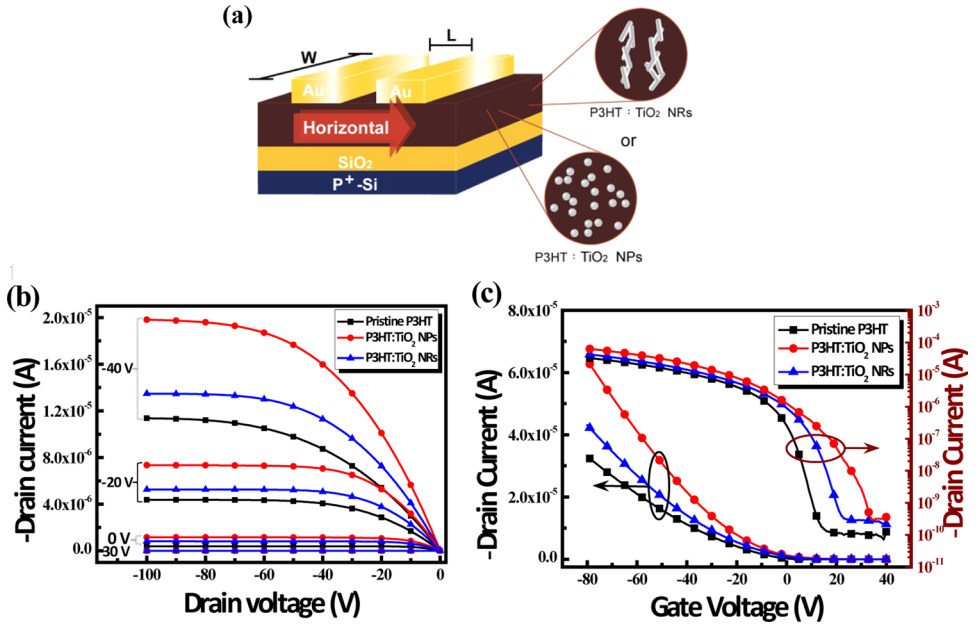

Figure 5. (a) Schematic illustration of thin film transistor (TFT) device structure. (b) Typical output characteristics ($-I_{DS}$ vs V_D) of pristine P3HT, P3HT:TiO_2 NPs, and P3HT:TiO_2 NRs-based TFTs operated at various V_G (−40, −20, 0, and 30 V). (c) Transfer characteristics ($-I_{DS}$ and logarithmic $-I_{DS}$ vs V_G) of pristine P3HT, P3HT:TiO_2 NPs, and P3HT:TiO_2 NRs-based TFTs operated at V_D = −90 V.

ratios (μ_h/μ_e) for the P3HT:TiO_2 NR and P3HT:TiO_2 NP hybrids are 1.7 and 2.7, respectively, indicating a more balanced carrier transport in P3HT:TiO_2 NR hybrid material which will be important for photovoltaic performance.

Next, we investigated the effect of nanocrystal dimensionality on the hole transport behavior in P3HT:TiO_2 hybrids along the direction parallel to the substrate by measuring the hole field-effect mobilities of pristine P3HT, P3HT:TiO_2 NPs, and P3HT:TiO_2 NRs hybrid films, based on a top-contact thin film transistor (TFT) geometry, as shown in Figure 5a. The details of device fabrications are described in the Experiments section. In this configuration, top Au source and drain electrodes were used to form an ohmic contact for horizontal hole injection. Figure 5b shows the typical output characteristics (drain current $-I_{DS}$ versus drain voltage V_D at a different gate voltage V_G) of pristine P3HT, P3HT:TiO_2 NP, and P3HT:TiO_2 NR-based transistor devices. Despite the addition of n-type TiO_2 nanocrystals into the P3HT matrix, all of these samples exhibit the typical transport characteristics of p-channel field-effect transistors. The $-I_{DS}$ of P3HT:TiO_2 NP- and P3HT:TiO_2 NR-based transistors are higher than that of the pristine P3HT-based transistor within all gate voltage ranges (operated at V_G = −40, −20, 0, and 30 V). Figure 5c shows the transfer characteristics ($-I_{DS}$ and logarithmic $-I_{DS}$ versus V_G) of these transistors at V_D = −90 V. An increase in drain current at zero gate voltage in both P3HT:TiO_2 nanocrystal hybrids was observed, suggesting that adding TiO_2 nanocrystals into the P3HT matrix might result in improved conductivity of the transistors. The horizontal hole field-effect mobilities of P3HT:TiO_2 NP and P3HT:TiO_2 NR hybrids are 0.175 and 0.105 $cm^2\ V^{-1}\ s^{-1}$, respectively, which are higher than 0.098 $cm^2\ V^{-1}\ s^{-1}$ of the pristine P3HT film. The on/off ratios of both BHJ-based transistors consisting of differently shaped TiO_2 nanocrystals are ~10^5, which is comparable with that of the pristine P3HT-based transistor. In contrast to the vertical transport behavior, the hole mobility along the direction parallel to the substrate in P3HT:TiO_2 NP hybrid device is higher than that in P3HT:TiO_2 NR counterpart. The enhancement of hole field effect mobility after adding nanocrystals in the P3HT has also been observed in other organic/inorganic hybrid systems.[33−35] Two possible mechanisms have been proposed to explain the enhanced hole field-effect mobility; the first is attributed to the reduction of trap density (N_T) in the conjugated polymer[33] after adding nanocrystals, and the second is caused by the improved crystallinity of the P3HT matrix as a result of the presence of nanocrystals.[35] Considering the morphological analyses based on GIXRD data and 3D tomography of P3HT:TiO_2 nanocrystal hybrids, the lamellar-stacking of P3HT crystallites in both P3HT:TiO_2 NP and NR hybrids were usually reduced after adding TiO_2 nanocrystals. The enhancement of hole field-effect mobility after adding TiO_2 nanocrystals may have been more possible because of the reduction of trap density (N_T), which is defined as[33]

$$N_T = \frac{-V_T C_{ox}}{q} \tag{4}$$

where V_T is the threshold voltage determined according to the x-intercept of the straight line in the $I_{DS}^{1/2}$ vs V_G plot, C_{ox} is the capacitance per unit area of the SiO_2 layer, and q is the elementary charge. We thus estimated the trap density (N_T) for P3HT:TiO_2 NP and P3HT:TiO_2 NR-based transistors of 5.15 × 10^{15} and 7.95 × 10^{15} m^{-2}, which are lower than 9.67 × 10^{15} m^{-2} of the pristine P3HT transistor; this is consistent with the observed trend of the enhanced hole mobility of P3HT after adding TiO_2 nanocrystals. Holes confined in the P3HT surrounded by the TiO_2 nanocrystals reduce the possibility of carrier recombination during transport, thereby decreasing the trap densities in both P3HT:TiO_2 NP and P3HT:TiO_2 NR-based transistors effectively. We found that TiO_2 NPs have more homogeneous dispersion in P3HT and the P3HT:TiO_2 NR hybrid is favored to form large-scale donor−acceptor separated phases as shown in the electron tomography image in Figure 3a. The addition of TiO_2 NPs, which are isotropic

dx.doi.org/10.1021/jp306921e | J. Phys. Chem. C 2012, 116, 25081−25088

without any preferred orientation, still maintains the predominant lamellar-stacking P3HT crystallites as compared to the P3HT:TiO_2 NR counterpart, enabling holes to transport more effectively along the P3HT thiophene chains stacking parallel to the substrate. However, our result of a higher hole field-effect mobility in P3HT:TiO_2 NP hybrid than in P3HT:TiO_2 NR hybrid is different from the result reported by ref 35, in which only TiO_2 NRs could cause an increase of the field-effect hole mobility of P3HT while the TiO_2 NPs decreased the mobility dramatically.[35] They observed the predominate edge-on P3HT domains in P3HT:TiO_2 NR hybrid film and alignment of P3HT chains along with TiO_2 NRs results in enhancing hole field-effect mobility. According to their model, a large number of TiO_2 NRs might be lying along the plane parallel to the substrate. By contrast, our 3D tomography image revealed that TiO_2 NRs in P3HT tend to form a large-scale donor−acceptor phase-separated morphology between two electrodes with preferred orientations angled toward the plane of the film. This may cause a significant decrease in lamellar stacking and an increase in the vertical stacking of P3HT, as compared to those in P3HT:TiO_2 NP hybrid. The discrepancy of our results, as compared to those in ref 35, might be attributed to various processing conditions or different solvents used in the film depositions.

4. CONCLUSION

In summary, we demonstrated the effect of nanocrystal dimensionality on the nanoscale morphology of polymers in P3HT:TiO_2 nanocrystal BHJs as well as its correlation to anisotropic optical absorption and carrier transport. The elongated and anisotropic TiO_2 nanorods in P3HT, which have preferred orientations angled toward the plane of the film, promote the formation of increased vertical-stacking of P3HT crystallites, as compared to P3HT:TiO_2 NPs hybrids, providing a more effective hole transport perpendicular to the substrate. The isotropic TiO_2 NPs, which have no preferred orientation and are more homogeneously dispersed in P3HT, result in a favorable hole transport behavior parallel to the substrate when compared to the P3HT:TiO_2 NRs hybrids. Our results provide crucial information in understanding the correlation of morphological, optical, and electronic properties for polymer/inorganic hybrid electronic devices.

■ ASSOCIATED CONTENT

Ⓢ Supporting Information

Figures S1−S3. This material is available free of charge via the Internet at http://pubs.acs.org.

■ AUTHOR INFORMATION

Corresponding Author

*E-mail: chunwei@ntu.edu.tw.

Notes

The authors declare no competing financial interest.

■ ACKNOWLEDGMENTS

This work is supported by National Science Council, Taiwan (Project No. NSC 99-2119-M-002-012- and 96-2112-M-002-030-MY3). C.H.D. is also thankful to NSRRC, Taiwan, for the arrangement of the beamtime.

■ REFERENCES

(1) Yu, G.; Gao, J.; Hummelen, J. C.; Wudl, F.; Heeger, A. J. *Science* **1995**, *270*, 1789−1791.
(2) Kim, Y.; Cook, S.; Tuladhar, S. M.; Choulis, S. A.; Nelson, J.; Durrant, J. R.; Bradley, D. D. C.; Giles, M.; Mcculloch, I.; Ha, C. S.; et al. *Nat. Mater.* **2006**, *5*, 197−203.
(3) Shaheen, S. E.; Brabec, C. J.; Sariciftci, N. S.; Padinger, F.; Fromherz, T.; Hummelen, J. C. *Appl. Phys. Lett.* **2001**, *78*, 841−843.
(4) Chen, H. Y.; Hou, J.; Zhang, S.; Liang, Y.; Yang, G.; Yang, Y.; Yu, L.; Wu, Y.; Li, G. *Nat. Photonics* **2009**, *3*, 649−653.
(5) Liang, Y.; Xu, Z.; Xia, J.; Tsai, S. T.; Wu, Y.; Li, G.; Ray, C.; Yu, L. *Adv. Mater.* **2010**, *22*, E135−E138.
(6) Huynh, W. U.; Dittmer, J. J.; Alivisatos, A. P. *Science* **2002**, *295*, 2425−2427.
(7) Mcdonald, S. A.; Konstantatos, G.; Zhang, S.; Cyr, P. W.; Klem, E. J. D.; Levina, L.; Sargent, E. H. *Nat. Mater.* **2005**, *4*, 138−142.
(8) Beek, W. J. E.; Wienk, M. M.; Janssen, R. A. J. *Adv. Mater.* **2004**, *16*, 1009−1013.
(9) Lin, Y. Y.; Chu, T. H.; Li, S. S.; Chuang, C. H.; Chang, C. H.; Su, W. F.; Chang, C. P.; Chu, M. W.; Chen, C. W. *J. Am. Chem. Soc.* **2009**, *131*, 3644−3549.
(10) Sun, B.; Marx, E.; Greenham, N. C. *Nano Lett.* **2003**, *3*, 961−963.
(11) Coakley, K. M.; McGehee, M. D. *Appl. Phys. Lett.* **2003**, *83*, 3380−3382.
(12) Ravirajan, P.; Peiró, A. M.; Nazeeruddin, M. K.; Graetzel, M.; Bradley, D. D. C.; Durrant, J. R.; Nelson, J. *J. Phys. Chem. B* **2006**, *110*, 7635−7639.
(13) Yang, X.; Loos, J.; Veenstra, S. C.; Verhees, W. J. H.; Wienk, M. M.; Kroon, J. M.; Michels, M. A. J.; Janssen, R. A. J. *Nano Lett.* **2005**, *5*, 579−583.
(14) Li, S. S.; Chang, C. P.; Lin, C. C.; Lin, Y. Y.; Chang, C. H.; Yang, J. R.; Chu, M. W.; Chen, C. W. *J. Am. Chem. Soc.* **2011**, *133*, 11614−11620.
(15) Oosterhout, S. D.; Wienk, M. M.; van Bavel, S. S.; Thiedmann, R.; Koster, L. J. A.; Gilot, J.; Loos, J.; Schmidt, V.; Janssen, R. A. J. *Nat. Mater.* **2009**, *8*, 818−824.
(16) van Bavel, S. S.; Sourty, E.; de With, G.; Loos, J. *Nano Lett.* **2009**, *9*, 507−513.
(17) Hindson, J. C.; Saghi, Z.; Hernandez-Garrido, J. C.; Midgley, P. A.; Greenham, N. C. *Nano Lett.* **2011**, *11*, 904−909.
(18) Lee, C. K.; Pao, C. W.; Chu, C. W. *Energy Environ. Sci.* **2011**, *4*, 4124−4132. Lee, C. K.; Pao, C. W.; Chen, C. W. *Energy Environ. Sci.* **2012**, DOI: 10.1039/C2EE23372.
(19) Todorov, I. T.; Smith, W. *The DL_POLY 4 User Manual*; STFC Daresbury Laboratory: Daresbury, 2011.
(20) Murgatroyd, P. N. *J. Phys. D: Appl. Phys.* **1970**, *3*, 151−156.
(21) Lee, S.; Moon, G. D.; Jeong, U. *J. Mater. Chem.* **2009**, *19*, 743−748.
(22) Ito, Y.; Virkar, A. A.; Mannsfeld, S.; Oh, J. H.; Toney, M.; Locklin, J.; Bao, Z. *J. Am. Chem. Soc.* **2009**, *131*, 9396−9404.
(23) Zhokhavets, U.; Gobsch, G.; Hoppe, H.; Sariciftci, N. S. *Thin Solid Films* **2004**, *451−452*, 69−73.
(24) Campoy-Quiles, M.; Etchegoin, P. G.; Bradley, D. D. C. *Phys. Rev. B* **2005**, *72*, 045209_1−045209_16.
(25) Erb, T.; Zhokhavets, U.; Gobsch., G.; Raleva, S.; Stühn, B.; Schilinsky, P.; Waldauf, C.; Brabec, C. J. *Adv. Funct. Mater.* **2005**, *15*, 1193−1196.
(26) Lilliu, S.; Agostinelli, T.; Pires, E.; Hampton, M.; Nelson, J.; Macdonald, J. E. *Macromolecules* **2011**, *44*, 2725−2734.
(27) Coakley, K. M.; Srinivasan, B. S.; Ziebarth, J. M.; Goh, C.; Liu, Y.; McGehee, M. D. *Adv. Funct. Mater.* **2005**, *15*, 1927−1932.
(28) Aryal, M.; Trivedi, K.; Hu, W. *ACS Nano* **2009**, *3*, 3085−3090.
(29) Ren, S.; Zhao, N.; Crawford, S. C.; Tambe, M.; Bulović, V.; Gradečak, S. *Nano Lett.* **2011**, *11*, 408−413.
(30) Sirringhaus, H.; Brown, P. J.; Friend, R. H.; Nielsen, M. M.; Bechgaard, K.; Langeveld-Voss, B. M. W.; Spiering, A. J. H.; Janssen, R. A. J.; Meijer, E. W.; Herwig, P.; et al. *Nature* **1999**, *401*, 685−688.

(31) Kim, D. H.; Park, Y. D.; Jang, Y.; Yang, H.; Kim, Y. H.; Han, J. I.; Moon, D. G.; Park, S.; Chang, T.; Chang, C.; et al. *Adv. Funct. Mater.* **2005**, *15*, 77−82.
(32) Chang, C. H.; Huang, T. K.; Lin, Y. T.; Lin, Y. Y.; Chen, C. W.; Chu, T. H.; Su, W. F. *J. Mater. Chem.* **2008**, *18*, 2201−2207.
(33) Xu, Z. X.; Roy, V. A. L.; Stallinga, P.; Muccini, M.; Toffanin, S.; Xiang, H. F.; Che, C. M. *Appl. Phys. Lett.* **2007**, *90*, 223509_1−223509_3.
(34) Chen, C. C.; Chiu, M. Y.; Sheu, J. T.; Wei, K. H. *Appl. Phys. Lett.* **2008**, *92*, 143105_1−143105_3.
(35) Sun, Z.; Li, J.; Liu, C.; Yang, S.; Yan, F. *Adv. Mater.* **2011**, *23*, 3648−3652.